PHILOSOPHICAL TRANSACTIONS A

*Phil. Trans. R. Soc. A.*

doi:10.1098/not yet assigned

# Observation of anomalous spectral downshifting of waves in the Okhotsk Sea Marginal Ice Zone

**Takuji Waseda[1]*, Alberto Alberello[3], Takehiko Nose[1], Takenobu Toyota[2], Tsubasa Kodaira[1], Yasushi Fujiwara[1]**

*[1]Graduate School of Frontier Sciences, the University of Tokyo, Kashiwa, 211-0066, Japan, https://orcid.org/0000-0001-5403-5303*

*[2] School of Mathematics, University of East Anglia, Norwich NR4 7TJ United Kingdom, https://orcid.org/0000-0001-7957-4012*

*[3]Low Temperature Institute, the Hokkaido University, Sapporo, Japan, https://orcid.org/0000-0003-1264-JMA, Tokyo*

**Keywords:** Marginal Ice Zone, wave attenuation, spectral downshifting, nonlinear wave interaction, wave modelling, ocean waves



## Summary

Waves in the Marginal Ice Zone in the Okhotsk Sea are less studied compared to the Antarctic and Arctic. In February 2020, wave observations were conducted for the first time in the Okhotsk Sea, during the observational program by Patrol Vessel Soya. A wave buoy was deployed on the ice, and in-situ wave observations were made by a ship-borne stereo imaging system and Inertial Measurement Unit. Sea ice was observed visually and by aerial photographs by drone, while satellite Synthetic Aperture Radar provided basin-wide spatial distribution. On 12 Feb., a swell system propagating from east northeast was detected by both the stereo imaging system and the buoy-on-ice. The wave system attenuated from 0.34 m significant wave height to 0.25 m in about 90 km while the wave period increased from 10 s to 15~17 s. This anomalous spectral downshifting was not reproduced by numerical hindcast and by applying conventional frequency-dependent exponential attenuation to the incoming frequency spectrum. The estimated rate of spectral downshifting, defined as a ratio of momentum and energy losses, was close to that of uni-directional wave evolution accompanied by breaking dissipation: this indicates that dissipation-driven nonlinear downshifting may be at work for waves propagating in ice.

*Author for correspondence (waseda@k.u-tokyo.ac.jp).

†Present address: Department, Institution, Address, City, Code, Country

# Introduction

The Okhotsk Sea experiences extensive freeze-up during winter ($5 - 7 \times 10^5$ km$^2$) but becomes completely ice-free during summer (Nihashi et al. 2018). Majority of sea ice in the Okhotsk Sea forms in the west where the fresh and warm water from the Amur River spreads (Wadhams 1986, Ogi et al. 2001). Then, the sea ice drifts south due to the East Sakhalin Currents (Ohshima et al. 2002), and from February to April, the sea ice is advected along Sakhalin Island and the coast of Hokkaido by the Soya Warm Current. As a result, the sea ice coverage is observed along the northeast of Hokkaido, for only a few months from January to March. Unlike the Arctic and Antarctic Ocean where the Marginal Ice Zone (MIZ) connects to multi-year or land-fast ice, the MIZ of the southwest Okhotsk Sea near Hokkaido is surrounded by open waters. Since 1996, an extensive observation program by Patrol Vessel Soya has been conducted every year by the Hokkaido University and the Japan Coast Guard. Based on the 20-year record, Toyota (Cruise Report SIRAS-20, ILTS 2020) identified that majority of the ice floe size in the south of Okhotsk Sea is around 2 m to 20 m and the level ice thickness is around 0.3 m to 0.7 m. The decades-long observations provided valuable data to identify deformed ice using Synthetic Aperture Radar data (Toyota et al. 2021) and to measure the floe size distribution of the small ice floes (Toyota et al. 2022). In 2020, the University of Tokyo joined the measurement program with a focus on wave measurements, conducted by stereo imaging, wave buoy on ice, and IMU (Inertial Motion Unit) measurement on the ship. Here we present the measured in-situ directional wave field. The observations are complemented by numerical wave model simulation to augment the information from the in-situ data.

In the Arctic Ocean and the Antarctic Ocean, many observational programs have been conducted aiming to estimate the rate of attenuation of the wavefield (Wadhams 1975, Squire and Moore 1980, Kohout et al. 2014, Thomson et al., 2018, Kodaira et al. 2020, Voermans et al. 2021, Montiel et al. 2022). Attenuation is a general term used to express how wave energy decreases with distance. Both conservative and non-conservative mechanisms exist, and the determination of which mechanism is at play is becoming a hot topic in the study of waves in ice (Voermans et al. 2019). The conservative wave scattering mechanism was pioneered by Wadhams (1975), and Fox and Squire (1994); the idea is to consider the diffraction of incoming waves by a solitary ice floe, hence assuming that the wavelength and the ice floe size are of the same order. The method of multiple diffractions from a distributed ice floe was elaborated by Peter and Meylan (2004) extending a scheme developed by Kagemoto and Yue (1986) who have considered the scattering of waves from 100s of surface piercing columns of an ocean platform. The theory was further extended by Kohout and Meylan (2008) to derive far-field solutions hence providing a transmission coefficient. The scattering process, therefore, provides a mechanism of wave attenuation in the propagation direction but the total energy is not lost from the system and a part of the wave energy is reflected in the incoming wave direction.

Another mechanism of attenuation is the dissipation of energy in the fluid boundary layer. Typically, a perturbation approach is taken such that the wave amplitude is considered only to provide a pressure field acting on the fluid interior, and the fluid boundary layer forms under stationary ice. Weber (1987) derived the attenuation rate which is equivalent to a rate of energy loss in the Stokes layer. Liu and Mollo-Christensen (1988) elaborated the theory and added a correction to the dispersion relation considering the thin elastic ice sheet. Both mechanisms assume a turbulent boundary layer and therefore introduce an eddy viscosity to explain the observed attenuation rate. The theory predicts the dependence of the attenuation rate on the wave frequency to be the power of 3.5, which is larger than the 2~2.7 predicted by the scattering mechanism. Such a frequency-dependent relationship acts as a benchmark to identify possible mechanisms at work and many recent studies show that the attenuation rate is close to satisfying the frequency to the power of 3.5 relations (Kodaira et al. 2020, Voermans et al. 2021, Meylan 2014, Meylan et al. 2018). There are other power laws resulting in the introduction of two viscous layers as well (Sutherland et all 2019). A

comprehensive review of wave propagation in ice including all the aforementioned studies is provided in this issue (Shen 2022).

Several recent works are in support of the turbulent boundary layer mechanism (Voermans et al. 2019, Smith and Thomson 2019), while others are in support of the scattering mechanism (Perrie et al. 2022). Moreover, the exponential decay of spectral energy may not represent true physics (Squire 2018). After all, energetics is not the only clue to identifying possible mechanisms at work. Alberello and Parau (2022) provided an interesting work on the interplay of linear viscous attenuation and nonlinearity related to spectral downshifting in the framework of weakly nonlinear narrow-banded spectral evolution. Alberello et al. (2021) documented observed spectral downshift in Antarctica. It may seem intuitive to assume that the spectral peak downshifts due to the frequency-dependent exponential attenuation: as a wave system propagates through the sea ice, high-frequency components get attenuated faster than the lower frequency components. As we show in this paper, however, frequency-dependent exponential attenuation cannot sufficiently explain the spectral downshifting observed in the Okhotsk Sea; the spectral peak shifted from 10 s to 15 s in 0.7 or less concentration ice over 90 km. In this study, we focus on how the spectral peak period changed as the waves propagated through the sea ice.

Spectral downshifting is the most notable characteristic of growing ocean waves. Staring from the study by Sverdrup and Munk (1946), the fetch law is still used as a benchmark to test the ocean models, as it is considered to govern the evolution of ocean waves. The downshifting is caused by nonlinear energy transfer among spectral components (Hasselmann 1962) and the approximate solution of the Boltzman's integral is implemented in the third-generation wave model. An alternative to this model was provided by Donelan et al. (2012) neglecting weak nonlinear interaction and assumed redistribution of energy due to energetic breaking waves. This idea of a dissipation-driven downshifting mechanism resonates to a certain extent with studies by Tulin (1996) and Tulin and Waseda (1999) where they claim imbalance of energy and momentum loss as the underlying principle of spectral downshifting. The fetch law based on the idea of the imbalance of energy and momentum loss was solved numerically by Fontaine (2013) demonstrating the validity of this idea. Waseda et al. (2009) showed that the imbalance is more pronounced when the directional spectrum becomes narrower, and the quasi-resonant interaction becomes dominant. Therefore, the dissipation-driven nonlinear downshifting mechanism may work for waves propagating under sea ice as the waves become more unidirectional.

The observations in the Okhotsk Sea were pointwise measurements from onboard the ship and the buoy on ice, as such they do not fully describe the evolution of waves. We, therefore, employed a numerical spectral wave model to extend the spatial coverage of the analysis. Although the model results deviated from the observations, the model does provide useful information. The model tuning was not attempted primarily because our analysis focuses not only on the energy but the momentum, which the model is unable to resolve but also, because of the large uncertainty in the forcing fields (Nose et al. 2018, Nose et al. 2020). Namely, the ice edge location differed considerably from the observed ice field by PALSAR. Moreover, while the PALSAR image shows heterogeneity of the ice field, the model only assumes a single type of ice field with constant ice thickness.

The motivation of this paper is to present two important messages for future work: i) the significance of spectral downshifting in the study of waves under ice and ii) the significance of the directional spectrum of waves under sea ice. These are poorly understood and should be further investigated.

# Methods

(a) Winter Okhotsk Sea Observation by PV Soya

Hokkaido University (HU) and Japan Coast Guard (JCG) have jointly conducted observations in the Okhotsk Sea since 1996 aboard the Patrol Vessel Soya. PV Soya is an ice breaker of length (LOA) of 98.6 m, beam (BOA) of 15.6 m, and 3,139 Gross tonnage (GT). This observation program led by Dr. Toyota of HU has repeated the observations along the same cruise line every winter for over 20 years. The research outcomes extend to physical, chemical, and biological oceanography and atmospheric science. Most recently Toyota et al. (2021) have reported the detection of deformed ice field from the SAR image (PALSAR) based on the observations by PV Soya from 2016 to 2019. The ice floe distribution from a drone aerial photograph has been conducted from the 2020 cruise (Toyota et al. 2022).

In 2020, wave observations were conducted from 10 to 15 Feb for the first time in the Okhotsk Sea: we deployed a wave buoy on ice from PV Soya, observed ice and wavefield by the stereo camera system, and measured the ship motion by IMU. These in-situ observations are described below together with the routine observations conducted during the HU-JCG joint observation by PV Soya.

(b) Satellite data

(i) AMSR2 sea ice concentration

The AMSR2 sea ice concentrations during the 2020 cruise are presented in Figure 1. The AMSR2-derived Sea Ice Concentration (SIC) was obtained from the ADS (Arctic Data archive System https://ads.nipr.ac.jp/) and is based on the Comiso bootstrap (BST) algorithm (Hori et al. 2012). From Fig.1, we can tell that the sea ice during the 2020 HU-JCG PV Soya observation period (10 to 15 Feb.) was advected southeast to the Shiretoko Peninsula and then veered northeast along the peninsula.

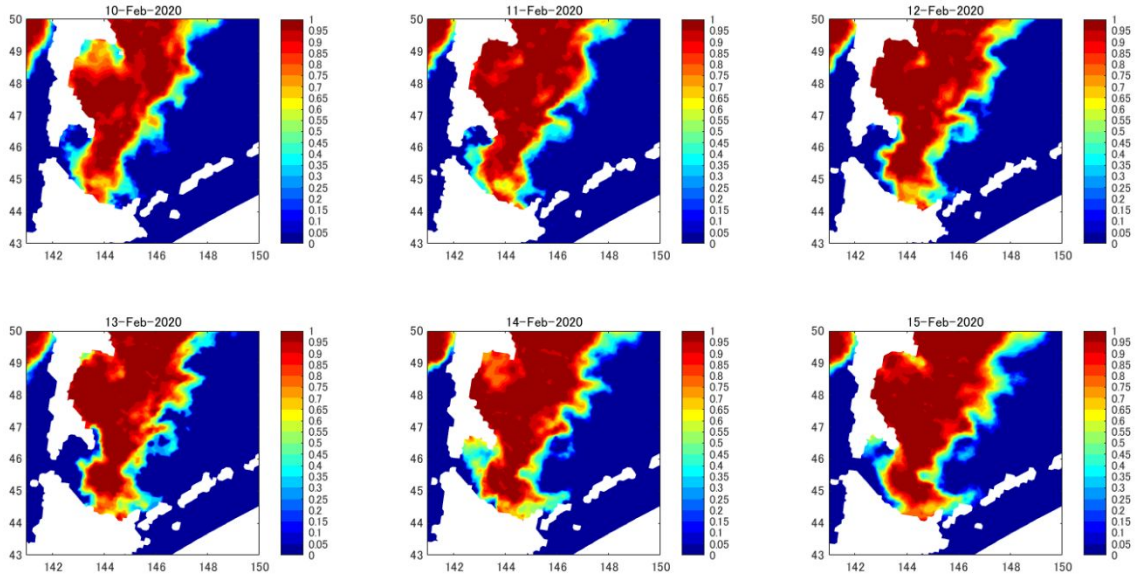


Figure 1: Daily AMSR2-derived Sea Ice Concentration (SIC) from 12 Feb (top left) to 15 Feb (bottom right). The colour shading changes at every 0.05 SIC. The horizontal axis is longitude and the vertical axis is latitude.

(ii) ALOS2/PALSAR image

AMSR2-derived SIC products are known to have large uncertainty depending on the analysis algorithm (Nose et al. 2020 and the references therein). An alternative sea ice field representation is Synthetic Aperture Radar (SAR) images. Figure 2 displays the ALOS2/Phased Array type L-band Synthetic Aperture Radar (PALSAR) image obtained on 10 Feb. 2020. The PALSAR image displays heterogeneity of the ice field (where open water and sea ice-covered seas are dappled) at

a scale undetectable by AMSR2. Moreover, an ice-band-like structure is observed in the MIZ, see Saiki et al. (2021). This PALSAR image will be used as a reference ice field for the 12 Feb. event when the largest wave was observed by the buoy on ice. Note that we removed the background gradient in the range from the original PALSAR image to reduce the incident angle dependency and scaled the adjusted normalized cross-section to greyscale from 0 to 255.

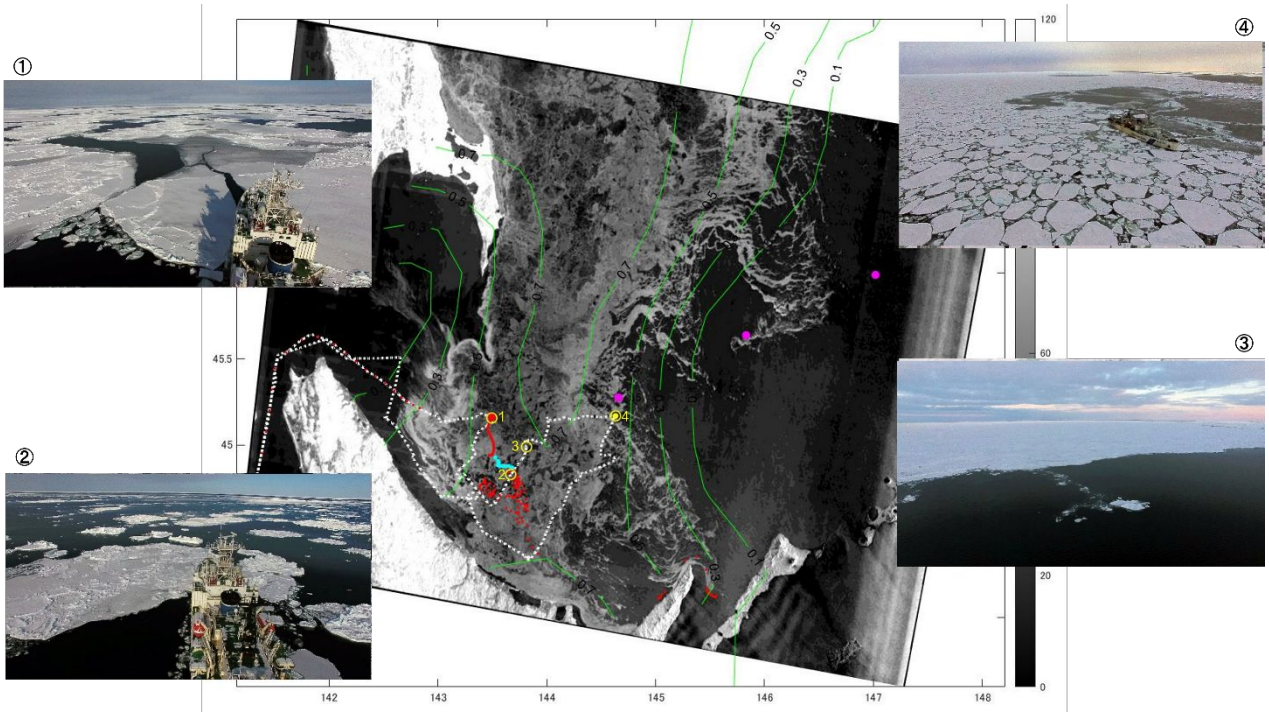


Figure 2: The ALOS-2/PALSAR image obtained on 10 Feb. 2020, is placed in the centre providing an overview of the sea ice distribution. The white dotted line traces the ship track of PV Soya from 9 Feb. to 15 Feb. 2020. The wave buoy was deployed on ice on 10 Feb. at the large solid redpoint and drifted freely to the south until the end of March when it lost connection in the Nemuro Strait (see the traces of red dots). The 12 Feb. wave event was observed at the points indicated in cyan. Stereo images were taken on the same day at a location indicated by a yellow solid dot. The sea ice condition varied a lot as depicted by the four drone images taken at locations 1 to 4 marked by yellow open circles. The magenta points are located along the 65-degree line from the buoy-on-ice (cyan points) and indicate where the directional spectra from TodaiWW3-OK were extracted. TodaiWW3-OK was forced by AMSR2-derived sea ice concentration indicated by the green contour lines.

(c) In-situ measurements:

(i) Aerial Drone images of the ice fields

Drone (DJI/PHANTOM4) images were taken from PV Soya at locations cutting across the ice field (locations are indicated by yellow open circles and numbered from 1 to 4 in the PALSAR image, Fig.2). The drone altitude was 50 m for all observations. Most images were taken at nadir looking angle to detect the ice floe size distribution (Toyota et al. 2022). Here we display images taken at a slanted angle to show a wider area. The images taken at six locations of which four of them are indicated by yellow circles are presented in Fig. 2. The PV Soya in the image provides the length scale (LOA 98.6 m, BOA 15.6 m). In location 1 (10 Feb. ~14:00 JST), the ice field consists of both relatively level ice floes and floes with ridges. Location 1 is where the wave buoy was deployed on the ice. In location 2 (11 Feb. ~14:00 JST), most of the ice floes were consolidated of smaller ice

floes. Therefore, the surface was rough. In location 3 (11 Feb. ~16:30 JST), large ice floes of a km scale were sparsely distributed. In location 4 (12 Feb. ~14:00 JST), a mixture of unconsolidated large and small ice floes was found and nilas filled the gaps.

(ii) Visual observation

Visual observation following the ASPeCt (Antarctic Sea-ice Processes and Climate) protocol was conducted every hour during the daytime. Observation records the total sea ice concentration (conc) and the types of ice (ty1, ty2, ty3), and their respective concentration (c1, c2, c3). Together with the video recording of the broken ice floes from the side of the ship, the sea ice size and thickness were estimated. Supplementary Table 1 summarizes the ASPeCt observations in locations 1 to 4 where the drone images were taken (indicated by yellow open circles in Figure 2).

(iii) Wave buoy on ice

Spotter wave buoy (SOFAR) was placed on a small ice floe (5 m radius) which PV Soya broke off from a larger ice floe (up to 100 m) as shown in Fig. 3 a. The location of the buoy deployment is indicated by the red large dot in Figure 2. A spotter wave buoy is a lightweight GPS-based wave sensor (Smit et al. 2021). To assure orientation of the buoy on ice, we have set it on a metal frame which should detach itself from the buoy and sink when the buoy is in the water. Typical of a GPS sensor, the background noise level drops off with frequency. The scale separation of the GPS background noise and the ocean wave allows the implementation of a high-pass filter to isolate the wave records (e.g. Waseda et al. 2014). Nevertheless, the signal-to-noise ratio of wave motion under sea ice is small because the wave period tends to be longer, and the amplitude tends to be small. We, therefore, identified a true wave signal from noise when the peak wave period does not deviate from the moment. The moment period is defined as $T_{0m} = \left(\int_{f_l}^{f_h} S(f)df \Big/ \int_{f_l}^{f_h} f^{-m} S(f)df\right)^{1/m}$ where $S(f)$ is the frequency spectrum $(f_l, f_h)$ is the integration interval, and $m$ is an integer.

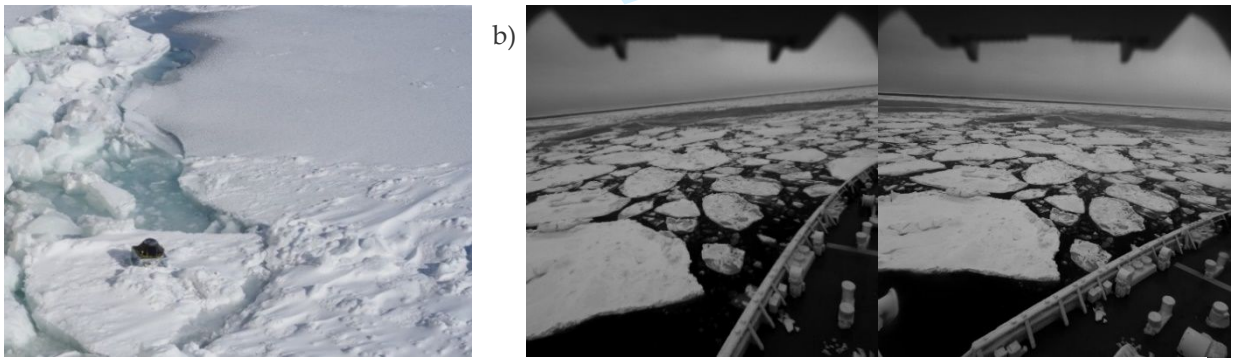


Figure 3 (a) Spotter buoy (SOFAR) was placed on an ice floe that was broken off from a larger ice floe. (b) A sample stereo image pair was taken from the upper deck of PV Soya.

(iv) Stereo imaging from the ship

Two CMOS cameras (Toshiba Teli BU406M (419M pixel 1/1, USB Bus synchronization), with CCTV lens (KOWA LM8HC 8mm 1"C Mount)) were set on the upper deck of PV Soya 2.96 m apart looking down on the water surface (Fig. 3 b). The cameras are located on the left side of the ship facing forward and slightly looking left observing the port-side waters (Supplementary Figure 1). From 10 to 15 Feb., 60 sequences of 20-minute records at 10 fps were obtained. Among 34 sequences suitable for processing, we have selected one sequence obtained around 12 Feb. 14:00 for 20 minutes when we encountered a swell propagation under the ice. The analysis was made using WASS (Waves Acquisition Stereo System) developed by Bergamasco et al. (2017). WASS is an automated software package that detects features on the water surface, calibrates the

external parameters of the stereo camera system, and reconstructs the wave field. The algorithm is designed to efficiently reconstruct the wave surface taking advantage that the displacement of the target is limited to the neighbourhood of the mean surface detected for each image. The reconstruction of the surface elevation covered by ice is not straightforward as described by Alberello et al. (2021). They have quantified the error of the stereo reconstructed wave field associated with the ship motion and concluded that the error is 0.5 % of the measured significant wave height. The error depends on the relative motion of the ship to the waves. In our observation, the spectral energy densities of the vertical motion measured by the IMU at the stereo camera location were negligible compared with the stereo reconstructed wave energy (supplementary Figure 2). The directional spectrum is estimated with the wavelet method from time series extracted from a virtual array within the field of view comprised of nine points in a radius of ≈2 m from the central one (Donelan et al. 1996). With ice in the field, detection of surface features becomes difficult and with the lack of viable observation points, two-dimensional Fourier analyses were not conducted. Moreover, the directional spectrum showed anomalous energy peaks in an unrealistic low frequency which is likely due to slow change in the ship direction. For further clarification of the recorded waves, a hand-held video image taken on Feb. 12 is provided as a supplementary material; for visibility of a 10 s wave, the frame rate is increased by five times.

(v) Ship-borne IMU

The ship heave motion was detected by the IMU (IMU-Z2 wireless motion sensor, ZMP) located on the upper deck where the stereo camera was placed. The sampling rate was 100 Hz and was recorded continuously during the cruise. The heave acceleration was integrated twice with a high-pass filter to obtain the heave motion of the PV Soya. IMU detected significant wave height and mean wave period are given in supplementary material (Supplementary Figures 3 and 4).

(d) WAVEWATCHIII hindcast simulation (TodaiWW3-OK)

The observational dataset was complemented with a wave hindcast experiment using the spectral wave model developed at the University of Tokyo (referred to as TodaiWW3-Okhotosk or TodaiWW3-OK in short herein) based on NOAA-WW3 (https://github.com/NOAA-EMC/WW3). NOAA-WW3 is known as a third-generation spectral wave model that solves the numerical evolution of ocean waves as energy ($E$) budgets based on the action density ($N \equiv E/\sigma$ where $\sigma$ is the intrinsic frequency) balance equation. Physical processes affecting the temporal and spatial wave spectral evolution are represented via source terms ($S_{tot}$), which consists of energy transfer from wind ($S_{in}$), breaking dissipation of energy ($S_{dis}$), attenuation of energy under the ice ($S_{ice}$), and nonlinear energy transfer among spectral components ($S_{nl}$):

$$\frac{\partial N}{\partial t} + \nabla \cdot \boldsymbol{c_g} N = \frac{S_{tot}}{\sigma} \quad (1)$$

$$S_{tot} = (1 - c_i)(S_{in} + S_{dis}) + c_i S_{ice} + S_{nl} \quad (2)$$

TodaiWW3-OK adopted the following source term parameterizations with the default setting: the ST6 physics package (Rogers et al., 2012, Zieger et al., 2015, Liu et al., 2019) for $S_{in}$ and $S_{dis}$, IC2 (Liu and Mollo-Christensen, 1988) for $S_{ice}$, and Discrete Interaction Approximation DIA (Hasslemann et al., 1985) for $S_{nl}$. Note that $S_{ice}$ represents wave attenuation by sea ice for both conservative and non-conservative mechanisms, but the TodaiWW3-OK simulations did not consider attenuation due to scattering. Furthermore, IC2 in its default model does not modify the open water dispersion relation in ice cover, then, the parameterization of the wave attenuation reverts to a model of Weber (1987) as it will be shown later. Details of the nested model configurations are given in the supplementary material (Supplementary Figure 5).

The sea ice concentration ($0 \leq c_i \leq 1$) plays a crucial role in evaluating the growth and decay of the waves under the ice-covered sea. The underlying assumption of (2) is that both the breaking dissipation and wind pumping are neglected under sea ice. This is fine for the dissipation as the attenuation of

waves under ice will be taken care of by $S_{ice}$. However, the neglect of wind pumping under the ice may become important for certain conditions, i.e., the waves may still grow under sea ice (Gemmrich et al. 2018, Thomson and Rogers 2014). Also, the modified dispersion relation is not used to evaluate the nonlinear energy transfer $S_{nl}$ (see Lavrenov 2003). Therefore, there are many missing or incomplete representations of the physical processes of waves propagating under sea ice (Thomson 2022 in this issue). Nevertheless, as Nose et al. (2020) has shown, the largest source of uncertainty in the model comes from the inaccurate representation of the ice edge and the concentration. In this paper, we will show that the $c_i$ used in this model deviates largely from the PALSAR image and the model was carefully used as a tool to augment the observational data analysis.

# Results

The buoy-on-ice deployed on 10 Feb. drifted south with the Soya current (see the red dots in Fig. 2) and on 11 Feb. to 13 Feb. (cyan dots in Fig. 2), swell propagation was detected, see Fig. 4 (a). The significant wave height was around 0.25 m, and the wave period was around 15 to 17 s (Fig. 4 (b)). The propagating direction (Fig. 4 (c)) was around 60 degrees or from the East Northeast. The directional spread narrowed from 11 Feb. 21:30 to 12 Feb. 14:00 (Fig. 4 (d)). We, therefore, identified that the waves observed during this period (denoted by red dots in Figs 4 (a) to (d)) as representing the same wave system. The frequency spectra during this period are shown in Fig. 4 (f) and their average is shown in Fig. 4 (e). The spectral peak changed in time and was either 0.059 Hz or 0.068 Hz. That is 17.1 s and 14.6 s, which is quite long considering that the waves were likely generated within the limited fetch of the Okhotsk Sea. In addition, considering the narrow directional spread of around 20 to 30 degrees (Fig. 4 (d)), the observed wave system is considered a swell.

The interest is to identify where this swell system originates. The direction of propagation is around 60 degrees (ENE) and coincidentally, we obtained the stereo images upstream around the same time in that direction (yellow solid dot in Fig. 2). Stereo image pairs were successfully analysed to produce surface elevation time series for the two cases presented in Fig. 5. The first case (Fig. 5 (a) 2/10 07:48) was obtained when the buoy was deployed on the ice. The second case (Fig. 5 (b) 2/12 13:48) detected the 12 Feb. event. Both cases show a group-like feature where the wave amplitude diminishes periodically. These time series were obtained at several locations in the imaging domain and the averaged frequency spectra for these cases are presented in Fig. 5 (c). The spectral peak frequency of the 10 Feb. case was 0.11 Hz or 8.9 s and the 2/12 case was 0.10 Hz or 9.5 s. The observed wave period was identical to the wave period obtained by the ship-borne IMU (supplementary Figure 4). The ambiguity of the main wave propagation direction was too large and possibly contaminated by the slight change in the ship heading during the observation. Now, we will focus on the 12 Feb. case (shown in red in Fig. 5), which represents the upwind condition for the observed swell event by the buoy-on-ice. From the variance of the surface elevation, the significant wave height was estimated to be around $H_s = 0.34$ m. The mean wave period obtained by the IMU was on average 9.1 s which is close to the peak frequency detected by the stereo reconstruction (Supplementary Figure 4).

Based on the buoy-on-ice observation and the ship-borne stereo image data, we conjecture that the, $H_s =$ 0.34 m and $T_p = 9.5$ s swell propagated into the MIZ and eventually transitioned to the swell of $H_s =$ 0.25 m and $T_p = 14.6$ s to 17.1 s (Table 1). The loss of energy was relatively small, only around 30 % attenuation, yet the spectral peak downshifted considerably (from around 10 s to 15~17 s). Such a large spectral downshift despite a moderate attenuation rate cannot be explained by conventional knowledge and deserves to be investigated. The observed spectral evolution is atypical compared to any observed wave attenuation under sea ice as the low-frequency wave energy grew at the expense of the wave energy at the peak of the incoming wave spectrum. It is apparent that dissipation cannot explain such growth, and a nonlinear energy transfer must be in action.

Table 1: Observed integrated wave parameters from the stereo image and the buoy on ice.

| | $H_s$ | $T_p$ | $f_p$ | $\lambda_p$ (open) | $ak_p$ | *direction* |
|---|---|---|---|---|---|---|
| Stereo image | 0.34 m | 9.5 s | 0.105 Hz | 140 m | 0.0076 | n/a |
| Buoy-on-ice | 0.25 m | 14.6 – 17.1 s | 0.059-0.066 Hz | 333-456 m | 0.0017-0.0024 | ~60 deg. |

The observation is limited to two points. To augment the missing information, we now investigate the wave model results. Here, we observe the wave spectra at the buoy-on-ice (cyan dots in Fig. 2) and where the stereo images were taken (the first magenta point), and further upwind along the ray for two more points (two magenta points upwind). The distance between the location of the stereo image capture and the buoy was around 82 to 91km. The model sampling distance (magenta points in Fig. 2) is roughly the same. A 10 s swell takes around 3 hours to propagate between these points, so we investigated the spectral evolution along the 65-degree line (connecting the cyan dots and magenta dots in Fig. 2) following the wave system in a Lagrangian manner by shifting the time by 3 hours.

The top row of Figure 6 shows the directional spectral evolution along the ray and the corresponding frequency spectra are shown in the bottom row. The location, time, significant wave height $H_s$, peak frequency $f_p$, peak period $T_p$ and energy period $T_{0m1}$ are summarized in Table 2. Within the frequency resolution of the spectra, $T_p$ ($f_p$) does not change despite the energy being attenuated to less than 10 % of that at the farthest point (270 km away from the buoy). Nevertheless, the attenuation of the high-frequency energy is higher than the low-frequency counterpart as depicted in the decrease of $T_{0m1}$. The directional spectra (Fig. 6 top row) show a peculiar bimodal distribution. It seems that the relatively high-frequency wave system propagating at around 30 to 40 degrees tends to attenuate faster and eventually the wave system at slightly low frequency propagating at around 60 degrees survives.

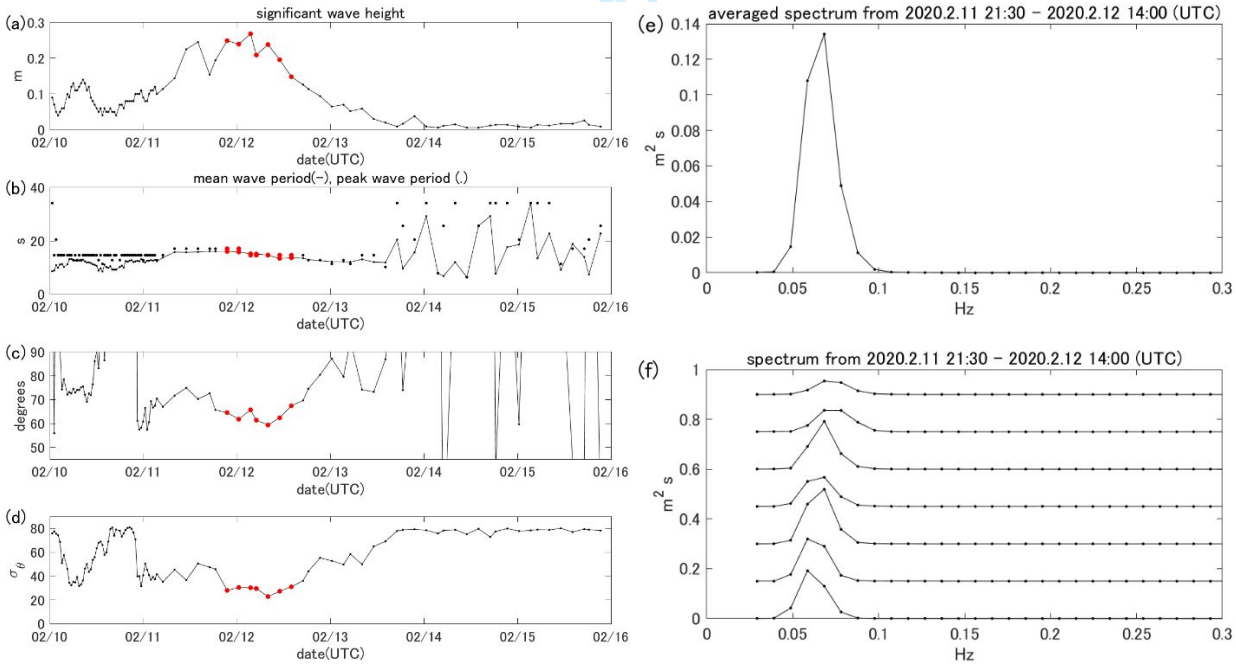


Figure 4: Buoy-on-ice derived a) significant wave height; b) mean and peak wave period; c) propagation direction; d) directional spread; e) averaged spectral energy density ($m^2s$) from the 7 spectra; and f) evolution of spectral energy density from 2020.2.11 21:30-2.12 14:00 (UTC), from bottom to top every 3

hours. The frequency resolution is 0.0098 Hz. The corresponding significant wave heights are 0.155 m, 0.20 m, 0.24 m, 0.21 m, 0.27 m, 0.24 m, and 0.25 m.

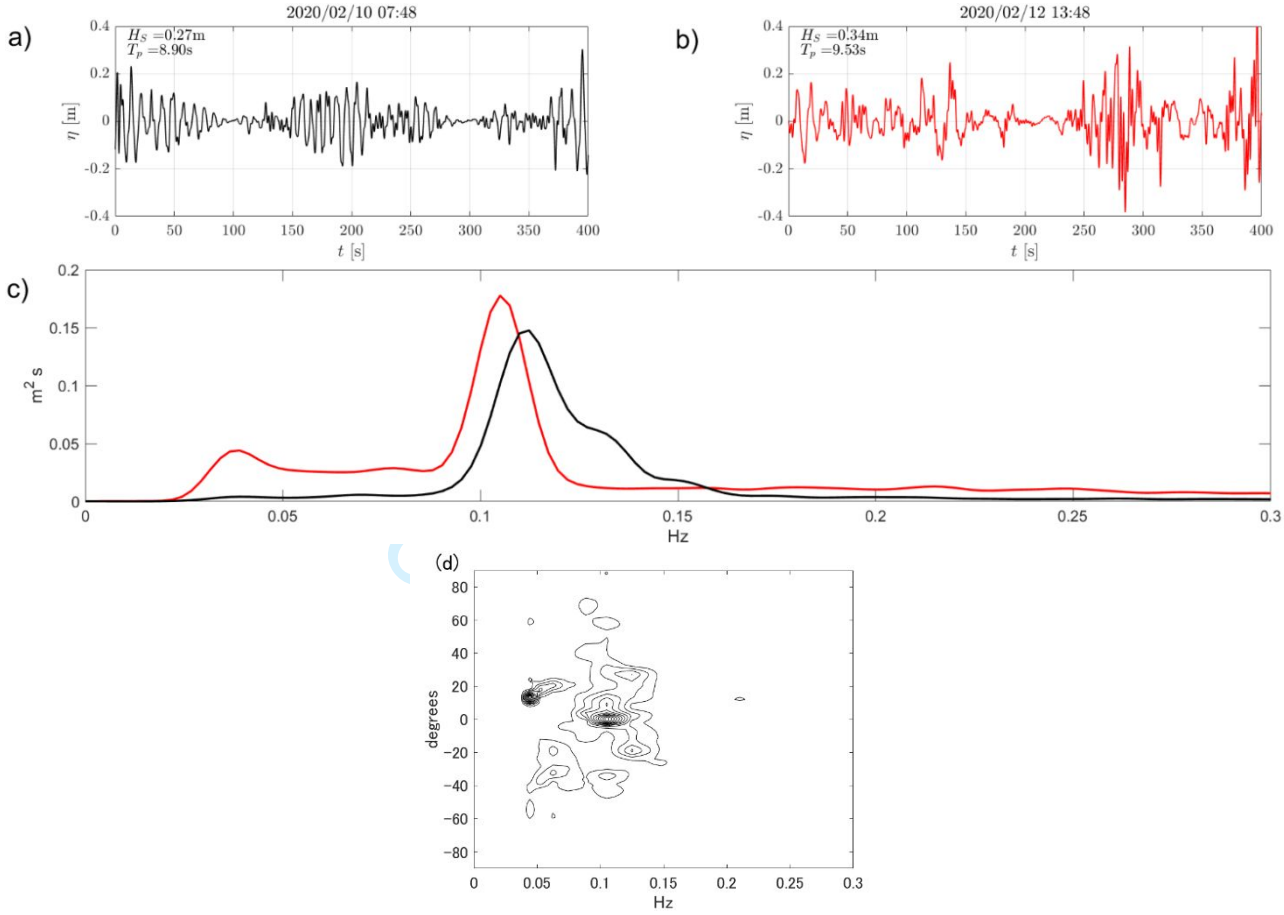


Figure 5: Stereo camera image sequences were analyzed to estimate the surface elevation time series for the two cases, 2020/2/10 07:48 and 2020/2/12/ 13:48. The top two figures (a and b) are sample time series from the estimate. Reconstruction of the surface elevation was successfully made, and the Fourier spectral densities were estimated as an ensemble average of those points; c) black for the 2/10 case and red for the 2/12 case. d) The selected 9-time series were used to estimate the directional spectral density.

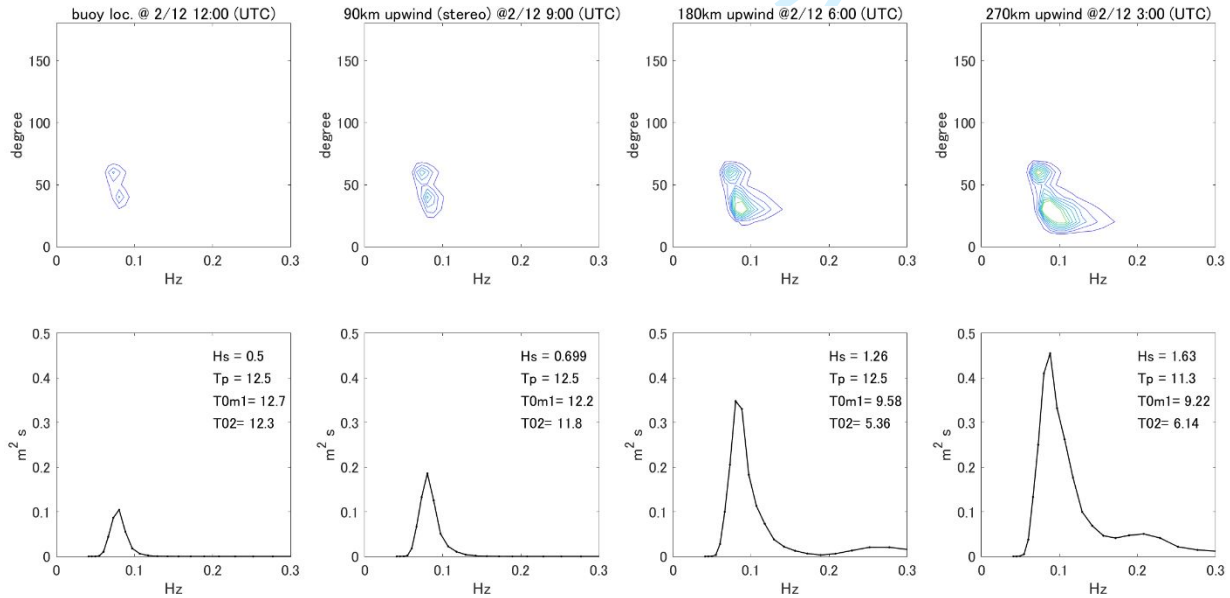

Figure 6: Directional spectra (top row) extracted from the TodaiWW3-OK at locations and times indicated in Table 2. The derived frequency spectral density ($m^2s$) are shown in the bottom row.

Table 2: Locations and times that the TodaiWW3-OK directional spectra were extracted. The derived integral parameters, significant wave height $H_s$, peak frequency $f_p$, peak period $T_p$, and energy period $T_{0m1}$ are listed.

| | buoy-on-ice | 90 km (Stereo camera) | 180 km | 270 km |
|---|---|---|---|---|
| lon/lat | 143.59/44.88 | 144.66/45.27 | 145.8/45.64 | 147.00/46.00 |
| time | 2/12 9:00 | 2/12 6:00 | 2/12 3:00 | 2/12 0:00 |
| $H_s$ | 0.500 m | 0.699 m | 1.26 m | 1.63 m |
| $f_p$ | 0.08 Hz | 0.08 Hz | 0.08 Hz | 0.088 Hz |
| $T_p$ | 12.5 s | 12.5 s | 12.5 s | 11.3 s |
| $T_{0m1}$ | 12.7 s | 12.2 s | 9.58 s | 9.22 s |

# Discussion

Wave attenuation under sea ice was first observed and modelled by Wadhams (1975) and further verified by Squire and Moore (1980). These pioneering works found that the exponential attenuation rate depended on wave frequency,

$$A \propto K_{20/27} f^{2\sim2.7} \quad (3)$$

Where $A$ is the attenuation coefficient defined by $a = a_0 exp(-Ax)$, $x$ is the distance from the initial position. The possible mechanism for this attenuation is multi-scattering by ice floes, in which the attenuation rate is proportional to the ratio of the reflection coefficient and the floe size; $A \propto pr/d$, where $p$ is the sea ice concentration, $r$ is the reflection coefficient, and $d$ is the floe size. Since the reflection coefficient $r$ decreases with the wavelength for a given floe size $d$, the attenuation rate reduces with wavelength.

The exponent is, however, smaller than the exponent that most recent operational wave models use based on the turbulent boundary layer theory,

$$A \propto K_{35} f^{3.5}. \quad (4)$$

Weber (1987) first derived this expression considering the wave attenuation under a viscous brash-like ice layer that is effectively not in a horizontal motion. By heuristic derivation, we can also show that this frequency dependence can be obtained by combining solutions of linear free surface wave (Airy wave) and a boundary layer that forms in an oscillatory flow (Stokes layer). The energy lost in the Stokes layer can be expressed as the time average of the work done by the surface force $p_{yx}u$, where $p_{yx}$ is the stress given by a first-order turbulence closure as $p_{yx} = 2\mu_e \frac{\partial u}{\partial y}$ where $\mu_e$ is the eddy viscosity. By considering the Stokes boundary layer underneath the ice, $u = Ue^{y\sqrt{\omega/2\nu_e}} cos\left(\omega t + y\sqrt{\omega/2\nu_e}\right)$, with a straightforward manipulation, the attenuation rate $\left(\frac{1}{2}\sqrt{\frac{\nu_e}{2}}\omega^{3.5} g^{-2}\right)$ can be rederived; here $\nu_e = \mu_e/\rho$ and $U = (ak)c$. This means that Weber's (1987) solution can be applied to waves under a solid ice sheet if we assume infinitesimal surface wave motion and the development of the Stokes boundary layer. The same attenuation rate was independently derived by Liu and Mollo-Chirstensen (1988) who have incorporated the dispersion relation of waves under the thin elastic plate. Alternatively, work by Sutherland et al (2019) introduces a moving viscous ice layer underneath the motionless surface layer and introduced a scaling law to derive the kinematic viscosity that depends on the wave frequency. As a result, the attenuation rate is proportional to frequency to the power of 4;

$$A \propto K_{40} f^4. \quad (5)$$

Interestingly, various theories end up providing different power laws of the attenuation rate $A \propto K_n f^n$, where $n$ ranges from 2 to 4. Recent work by Voermans et al (2021) summarized relevant observational results and suggests that the exponent of the power-law may be related to the ice types including grease ice (Kodaira et al. 2020), broken pack ice (Kohout and Williams 2013), pancake ice (Thomson et al., 2018) and landfast ice (Voermans et al. 2021).

In this study, we are not aiming to benchmark the value of $n$ based on energy attenuation. Rather we provide a different perspective on how we may identify the most relevant physical process when waves are propagating in ice, that is to investigate the spectral downshifting. For that, we first conduct a simple exercise of estimating the rate of spectral downshifting of a Gaussian spectrum with attenuation:

$$a(x) = a_0 \exp\left(-\frac{(f-f_p)^2}{\sigma^2}\right)\exp\left(-K_n f^n x\right) \quad (6)$$

Initially, $x = 0$, $\sigma$ is the frequency bandwidth, and the spectral peak is $f_p$. As the waves propagate and attenuate, the spectral peak $f_{dp}$ downshifts satisfying

$$-2\frac{(f_{dp}-f_p)}{\sigma^2} - nK_n x {f_{dp}}^{n-1} = 0 \quad (7)$$

The rate of downshifting, as introduced in Waseda et al. (2009) to represent the relative magnitude of momentum loss and energy loss,

$$\Gamma \equiv \frac{df_{dp}}{dx}\frac{1}{f_{dp}} \Big/ \left(\frac{dE/dx}{E}\right) \quad (8)$$

can be approximated for the Gaussian spectrum with attenuation as

$$\Gamma \sim \frac{n}{2}\sigma^2 {f_p}^{-2}. \quad (9)$$

Therefore, spectral downshift due to dissipation in the boundary layer becomes larger as the exponent $n$ of the frequency dependence of the attenuation rate increases. Moreover, the spectral downshift is large for a broader spectrum, but for a narrow spectrum, becomes small.

We now investigate the observed spectral downshift. We consider the spectrum obtained by the stereo reconstruction as an initial condition (Figure 7, black solid line) and the buoy-on-ice observation as the attenuated wave field (Fig. 7 red solid line). Recall that the significant wave height reduced from 0.34 m to 0.25 m, while the peak period reduced from around 10 s to 16 s in about 90 km (Table 1). The exponential attenuation rate $dln\left({H_s(x)}/{H_s(0)}\right)/dx \approx -4.2 \times 10^{-6}\, m^{-1}$ is close to the estimation by Kohout et al. (2020), $dH_s/dx = -0.5 \times 10^{-5} H_s$ for $IC \leq 80, T_p \leq 14, H_s \leq 8$. Therefore, the observed attenuation rate seems to be consistent with the past observations.

Next, we apply frequency-dependent attenuation to the observed frequency spectrum where the exponential attenuation rate $A = K_n f^n$ is expressed as in (3) to (5) (Fig.7 orange, green, blue, and magenta solid lines). The coefficient $K_n$ was adjusted such that the attenuated $H_s$ is around 0.25 m for each relation. The main peak of the spectrum hardly downshifts. As given in (9), the downshift is small for a narrow (small $\sigma$) spectrum. Furthermore, empirical attenuation rates were applied (Fig. 7 dashed lines in color). Thomson et al. (2021) summarizes five empirical relations from observations; CODA 2019 (Hosekova et al., 2020)., SeaState 2015 (Thomson et al., 2018), SIPEX 2012 (Kohout et al. 2014), STiMPI 2000 (Doble et al. 2015), Greenland Sea 1978 (Wadhams et al. 1988). When those empirical relations were used, the wave attenuations were mostly too large, except for the cases from CODA 2019 ($H_s = 0.11\, m$) and SIPEX 2012 ($H_s = 0.096\, m$) in which energy from the main peak is completely lost, spectral downshift is hardly observed. In summary, we were not able to explain the transition from the spectrum obtained by the stereo-camera to the spectrum from the buoy-on-ice (red line) by applying exponential attenuation.

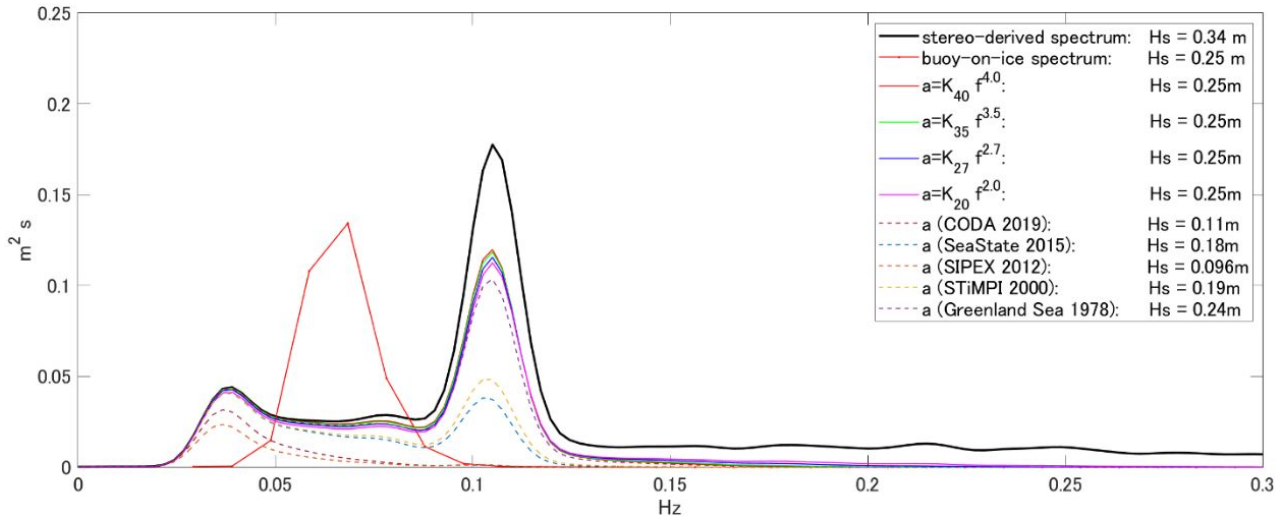


Figure 7: Attenuation of observed wave spectral energy density by various exponential attenuation coefficients: $A = K_n f^n$ with $n = 2.0, 2.7, 3.5, 4.0$, and empirical formulas summarized in Thomson et al. (2021), CODA 2019, SeaState 2015, SIPEX 2012, STiMPI 2000, Greenland Sea 1978. The observed buoy-on-ice spectral energy density is presented in a red solid line.

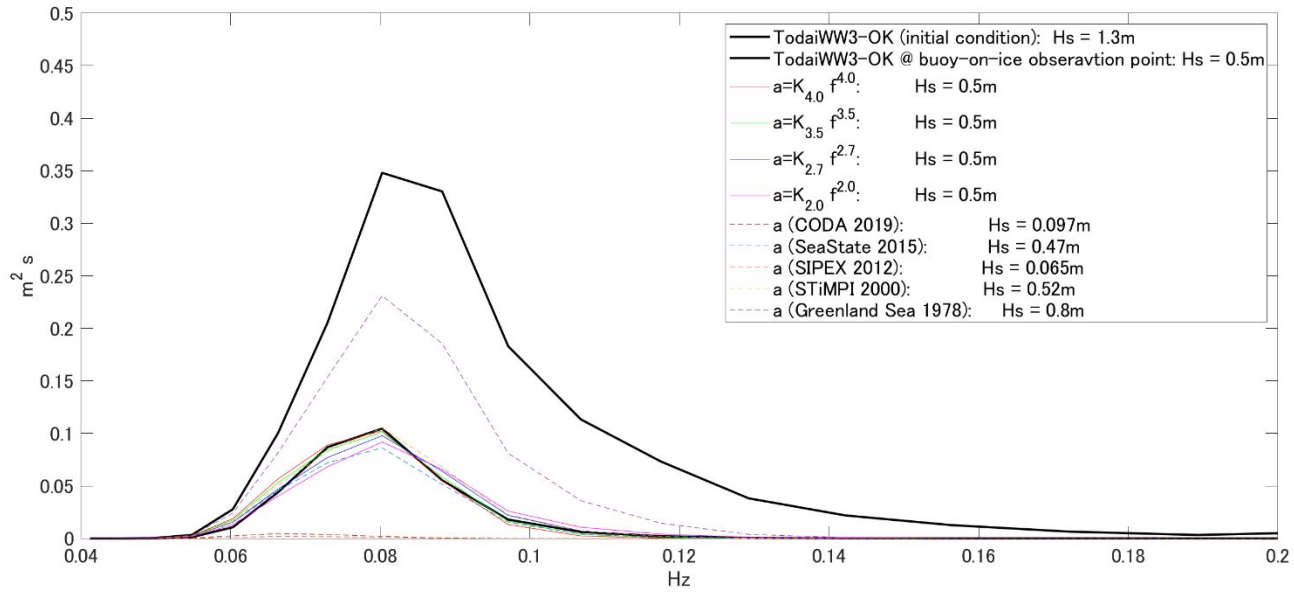


Figure 8: Attenuation of simulated wave spectral densities by various exponential attenuation coefficients: $A = Kf^n$ with $n = 2.0, 2.7, 3.5, 4.0$, and empirical formulas summarized in Thomson et al. (2021), CODA 2019, SeaState 2015, SIPEX 2012, STiMPI 2000, Greenland Sea 1978. The initial condition from TodaiWW3-OK was 180 km away from the buoy location and TodaiWW3-OK spectral density at the buoy-on-ice observation point is plotted in black thick solid lines. Spectral energy density values are given in $m^2s$.

We now analyse the spectral evolution from TodaiWW3-OK (Figure 6). The model failed to replicate the observed significant wave height, period, and spectra, but the result can be analysed to scrutinize the underlying downshifting mechanism. We repeat the same procedure of applying exponential attenuation to the initial condition taken from the simulated spectrum and observe how the spectrum changes (Figure 8). We took the point 180 km from the buoy as an initial condition located close to the model forcing ice edge (see Fig. 2). The use of $A = K_n f^n$ with the coefficient $K_n$ adjusted such that the attenuated $H_s$ is around

0.5 m resulting in a good replication of the spectrum at the buoy observation location (cyan dots in Fig. 2). By close inspection, it seems that the case with $n = 3.5$ agrees best with the model result (green solid line). This is not surprising as the wave-ice interaction package we used employed Weber's formula for the attenuation, equation (4).

From the results presented in Figs 7 and 8, we may conclude that the exponential attenuation of spectral wave components based on multiple wave scattering and energy loss at the fluid boundary layer cannot explain the anomalous spectral downshift observed in the Okhotsk Sea (downshift of peak period from 10 s to 15~17 s in 90 km). We now apply the observed wave parameters to the rate of downshifting (8). We obtain $\Gamma = 0.82$ which exceeds the largest value observed in a directional wave tank (the range was $\Gamma \sim 0.2 - 0.6$, Waseda et al. 2009). They have suggested that a large value of $\Gamma$ is attained when quasi-resonant nonlinear interaction becomes significant for a directionally narrow spectrum. Indeed, the directional spread of the spectrum observed by the buoy-on-ice was narrow, around 20 to 30 degrees. Overall, we may suggest that nonlinear interaction may have played a crucial role in the observed anomalous downshifting of the spectrum. However, it should be noted that the nonlinearity as represented by the steepness is quite low (Table 1). With steepness $ak \sim O(10^{-2})$ to $O(10^{-3})$, the dynamic time scale, $O((ak)^{-2}T) \sim 10^4$ *to* $10^6$ wave periods are much longer than the propagation time scale of around 1000 wave periods. Tulin (1995) and Donelan et al. (2012) have presented the possibility of a dissipation-driven nonlinear energy transfer mechanism, while Tulin and Waseda (1999) experimentally quantified the imbalance of momentum and energy loss due to energetic plunging breaker to obtain values of $\Gamma \sim 0.4$. In addition, Waseda et al. (2009) have shown that such dissipation-driven nonlinear energy transfer is enhanced with a directionally narrow spectrum. Based on these past studies, we can postulate a possible scenario of dissipation-driven nonlinear downshifting of waves in ice. As the waves propagate in the MIZ, waves scatter and simultaneously lose energy. As a result, the directional spectrum narrows, and concurrently the balance of energy and momentum is lost. This is speculation at this point, and we need observational evidence on the directional spectral evolution in ice. An outstanding question is the dissipation mechanism at work. Processes that are not considered yet and may need to be considered are energy loss due to collisions of ice floes (Shen et al. 1987), overwash over thin ice sheets (Nelli et al. 2020), and other mechanical losses related to large deformation of ice such as ridging, rafting, and ice floe fracture (Squire 2020).

Lastly, we should note that observations of waves around 15 s or so are not limited to this event on 12 Feb. 2020. Visual and recent instrumental observations during the repeated Sea Ice Research Activities by P/V Soya (SIRAS) cruises report the presence of such long-period waves. The emergence of such long-period waves despite limited fetch and storm activity in the Okhotsk Sea cannot be explained without the influence of sea ice. The distribution of sea ice in the Okhotsk Sea MIZ is unique. Unlike the Arctic and Antarctica where the MIZ is connected to multi-year and land-fast ice such that the attenuation rate increases as the waves propagate into the MIZ, the MIZ in the Okhotsk Sea is surrounded by open water. For example, the sea ice concentration of the MIZ along the wave propagation direction peaked around 0.7 and decreased for the observations presented in this study. This unique feature of the sea ice distribution in the northeast of Hokkaido makes this MIZ distinct from Arctic and Antarctic MIZs.

Uncertainty remains in the analysis. The most important question is to prove whether the two observed wave systems, one by the buoy-on-ice and the other by the ship-borne stereo imaging system, are the same system. Coincidentally, the stereo images were taken along the main wave propagation direction (60 degrees, ENE) from the wave buoy. However, the stereo images were not able to identify the absolute direction of wave propagation. We, therefore, relied on the numerical wave model to provide the directional information. However, it turns out that the directional spectrum of the simulated wavefield was bimodal and two wave systems propagating from 60 degrees (ENE) and around 30 degrees (NNE) coexisted. According to the weather condition during that time (12 Feb. 2020), there was a strong Northerly wind in the northeast of Sakhalin. Swell may have propagated from the distant gale condition from the

NNE which the model seems to have replicated. Considering that the sea ice condition varied largely across the MIZ (see Fig. 2), the spatial gradient of the ice type may result in large refraction of wave propagation. The process of wave refraction in ice is not considered in models that assume constant ice conditions. Therefore, the origin of the wave system remains uncertain.

# Conclusions

Wave observations were conducted for the first time in the MIZ that appears for only a few months in the northeast of Hokkaido. The Okhotsk Sea MIZ is characterized by the southward drift of sea ice by the Soya current and incoming waves from the east and north regions. In February 2020, during the observational program by the Hokkaido University and Japan Coast Guard, we deployed a wave buoy on ice and conducted stereo imaging of sea ice and waves from PV Soya. These two instruments detected a swell system on 12 Feb., where the incoming waves from the east were detected by the stereo camera system, and the attenuated waves by the buoy-on-ice to the west. The incoming significant wave height of 0.34 m was attenuated to 0.25 m in about 90 km, and the wave period increased from around 10 s to 15-17 s. This anomalous spectral downshifting was not able to be explained by the frequency-dependent attenuation rate regardless of the choice of the exponent. Therefore, neither the multi-scattering nor the boundary layer dissipation mechanisms succeeded in explaining the downshifting. On the other hand, the spectral downshifting of the modelled wavefield was well explained by the boundary layer dissipation, which is not surprising as the model attenuation rate was based on the boundary layer dissipation. For the observed wave system, the rate of downshifting that represents an imbalance of the momentum loss and energy loss was around 0.8 which is on the high-end of the experimental values obtained from nearly unidirectional spectral evolution in a wave tank. With these results, we hypothesize that the dissipation-driven nonlinear process may be responsible for the anomalous downshifting observed in the Okhotsk Sea MIZ. More work is warranted in improving the detection of the directional wave spectra to clarify the origin of the incoming waves and the possible nonlinear interaction occurring in the MIZ.

## Acknowledgments

Observations in the Sea of Okhotsk were conducted by Hokkaido University in collaboration with Japan Coast Guard, PV “Soya.” TW acknowledges M. Ito and J. Nishioka for their assistance in deploying the buoy on ice. The participation in the Soya cruise was initiated through the research collaboration sponsored by the Institute of Low Temperature Science of Hokkaido University. A part of the research was conducted under the Arctic Challenge for Sustainability II (MEXT) and Kakenhi (JSPS) 19H00801, 19H05512. ALOS-2/PALSAR-2 images were provided by Japan Aerospace Exploration Agency (JAXA) through the 2nd Research Project on the Earth Observations (PI: ER2A4N012). AA was supported by the Japanese Society for the Promotion of Science (PE19055).

# References

1. Alberello, A., Bennetts, L., Onorato, M., Vichi, M., MacHutchon, K., Eayrs, C., ... & Nelli, F. (2021). Three-dimensional imaging of waves and floe sizes in the marginal ice zone during an explosive cyclone. arXiv preprint arXiv:2103.08864.
2. Alberello, A., & Părău, E. I. (2022). A dissipative nonlinear Schrödinger model for wave propagation in the marginal ice zone. Physics of Fluids, 34(6), 061702.
3. Bennetts, L. G., and V. A. Squire (2012), On the calculation of an attenuation coefficient for transects of ice-covered ocean, Proc. R. Soc. A, 468(2137), 136–162.

4. Bergamasco, F., Torsello, A., Sclavo, M., Barbariol, F., & Benetazzo, A. (2017). WASS: An open-source pipeline for 3D stereo reconstruction of ocean waves. Computers & Geosciences, 107, 28-36.
5. Doble, M. J., De Carolis, G., Meylan, M. H., Bidlot, J.-R., & Wadhams, P. (2015). Relating wave attenuation to pancake ice thickness, using field measurements and model results. Geophysical Research Letters, 42(11), 4473–4481. https://doi.org/10.1002/2015GL063628
6. Donelan, M. A., Drennan, W. M., & Magnusson, A. K. (1996). Nonstationary analysis of the directional properties of propagating waves. Journal of Physical Oceanography, 26(9), 1901-1914. https://doi.org/10.1175/1520-0485(1996)026<1901:NAOTDP>2.0.CO;2
7. Donelan, M. A., Curcic, M., Chen, S. S., & Magnusson, A. K. (2012). Modeling waves and wind stress. Journal of Geophysical Research: Oceans, 117(C11). https://doi.org/10.1029/2011JC007787
8. Fontaine, E. (2013). A theoretical explanation of the fetch-and duration-limited laws. Journal of Physical Oceanography, 43(2), 233-247. https://doi.org/10.1175/JPO-D-11-0190.1
9. Fox, C., & Squire, V. A. (1994). On the oblique reflexion and transmission of ocean waves at shore fast sea ice. Philosophical Transactions of the Royal Society of London. Series A: Physical and Engineering Sciences, 347(1682), 185-218. https://doi.org/10.1098/rsta.1994.0044
10. Gemmrich, J., Rogers, W. E., Thomson, J., & Lehner, S. (2018). Wave evolution in off‐ice wind conditions. Journal of Geophysical Research: Oceans, 123(8), 5543-5556. https://doi.org/10.1029/2018JC013793
11. Hasselmann, K. (1962). On the non-linear energy transfer in a gravity-wave spectrum Part 1. General theory. Journal of Fluid Mechanics, 12(4), 481-500. https://doi.org/10.1017/S0022112062000373
12. Hasselmann, S., and K. Hasselmann (1985), Computations and parameterizations of the nonlinear energy transfer in a gravity-wave spectrum, Part I: A new method for efficient computations of the exact nonlinear transfer integral, J. Phys. Oceanogr., 15, 1,369–1,377. https://doi.org/10.1175/1520-0485(1985)015<1369:CAPOTN>2.0.CO;2
13. Hosekova, L., Malila, M. P., Rogers, W. E., Roach, L. A., Eidam, E., Rainville, L., et al. (2020). Attenuation of ocean surface waves in pancake and frazil sea ice along the coast of the chukchi sea. Journal of Geophysical Research: Oceans, 125(12), e2020JC016746. https://doi.org/10.1029/2020JC016746
14. Institute of Low Temperature Science (2020). Sea Ice Research Activities by P/V Soya in 2020 (SIRAS-20), Cruise Report volume 17
15. Jensen, J. J., Mansour, A. E., & Olsen, A. S. (2004). Estimation of ship motions using closed-form expressions. Ocean Engineering, 31(1), 61-85. https://doi.org/10.1016/S0029-8018(03)00108-2
16. Kagemoto, H., & Yue, D. K. (1986). Interactions among multiple three-dimensional bodies in water waves: an exact algebraic method. Journal of fluid mechanics, 166, 189-209. https://doi.org/10.1017/S0022112086000101
17. Kohout, A. L., & Meylan, M. H. (2008). An elastic plate model for wave attenuation and ice floe breaking in the Marginal Ice Zone. Journal of Geophysical Research: Oceans, 113(C9). https://doi.org/10.1029/2007JC004434
18. Kohout, A., Williams, M., Dean, S. et al. (2014) Storm-induced sea-ice breakup and the implications for ice extent. Nature 509, 604–607. https://doi.org/10.1038/nature13262
19. Kohout, A. L., Smith, M., Roach, L. A., Williams, G., Montiel, F., & Williams, M. J. (2020). Observations of exponential wave attenuation in Antarctic sea ice during the PIPERS campaign. Annals of Glaciology, 61(82), 196-209. https://doi.org/10.1017/aog.2020.36
20. Kodaira, T., Waseda, T., Nose, T., Sato, K., Inoue, J., Voermans, J., & Babanin, A. (2021). Observation of on-ice wind waves under grease ice in the western Arctic Ocean. Polar Science, 27, 100567. https://doi.org/10.1016/j.polar.2020.100567
21. Lavrenov, I. (2003). Wind-waves in oceans: dynamics and numerical simulations. Springer Science & Business Media. ISBN: 978-3-662-05146-7
22. Liu, A. K., & Mollo-Christensen, E. (1988). Wave propagation in a solid ice pack. Journal of physical oceanography, 18(11), 1702-1712. https://doi.org/10.1175/1520-0485(1988)018<1702:WPIASI>2.0.CO;2

23. Liu, Q., Rogers, W. E., Babanin, A. V., Young, I. R., Romero, L., Zieger, S., Qiao, F., and Guan, C. (2019). Observation-Based Source Terms in the Third-Generation Wave Model WAVEWATCH III: Updates and Verification. *Journal of Physical Oceanography* 49, 2, 489-517, https://doi.org/10.1175/JPO-D-18-0137.1
24. Meylan, M. H., Bennetts, L. G., & Kohout, A. L. (2014). In situ measurements and analysis of ocean waves in the Antarctic Marginal Ice Zone. Geophysical Research Letters, 41(14), 5046-5051. https://doi.org/10.1002/2014GL060809
25. Meylan, M. H., Bennetts, L. G., Mosig, J. E. M., Rogers, W. E., Doble, M. J., & Peter, M. A. (2018). Dispersion relations, power laws, and energy loss for waves in the marginal ice zone. Journal of Geophysical Research: Oceans, 123(5), 3322-3335.
26. Montiel, F., Kohout, A. L., & Roach, L. A. (2022). Physical drivers of ocean wave attenuation in the Marginal Ice Zone. Journal of Physical Oceanography. https://doi.org/10.1175/JPO-D-21-0240.1
27. Nelli, F., Bennetts, L. G., Skene, D. M., & Toffoli, A. (2020). Water wave transmission and energy dissipation by a floating plate in the presence of overwash. Journal of Fluid Mechanics, 889.
28. Nihashi, S., Kurtz, N., Markus, T., Ohshima, K., Tateyama, K., & Toyota, T. (2018). Estimation of sea-ice thickness and volume in the Sea of Okhotsk based on ICESat data. Annals of Glaciology, 59(76pt2), 101-111. doi:10.1017/aog.2018.8
29. Nose, T., Webb, A., Waseda, T. et al. (2018) Predictability of storm wave heights in the ice-free Beaufort Sea. Ocean Dynamics 68, 1383–1402. https://doi.org/10.1007/s10236-018-1194-0
30. Nose, T., Waseda, T., Kodaira, T., & Inoue, J. (2020). Satellite-retrieved sea ice concentration uncertainty and its effect on modelling wave evolution in Marginal Ice Zones. The Cryosphere, 14(6), 2029-2052. https://doi.org/10.5194/tc-14-2029-2020
31. Ogi, M., Tachibana, Y., Nishio, F., & Danchenkov, M. A. (2001). Does the fresh water supply from the Amur River flowing into the Sea of Okhotsk affect sea ice formation?. Journal of the Meteorological Society of Japan. Ser. II, 79(1), 123-129. https://doi.org/10.2151/jmsj.79.123
32. Ohshima, K. I., Wakatsuchi, M., Fukamachi, Y., and Mizuta, G. (2002). Near-surface circulation and tidal currents of the Okhotsk Sea observed with satellite-tracked drifters, J. Geophys. Res., 107( C11), 3195, doi:10.1029/2001JC001005
33. Passerotti, G., Bennetts, L. G., Alberello, A., Puolakka, O., Dolatshah, A., Monbaliu, J., & Toffoli, A. (2021). Interactions between irregular wave fields and sea ice: A physical model for wave attenuation and ice break up. arXiv preprint arXiv:2110.12659. (accepted for publication, J. of Phys. Oceanogr.)
34. Peter, M. A., & Meylan, M. H. (2004). Infinite-depth interaction theory for arbitrary floating bodies applied to wave forcing of ice floes. Journal of Fluid Mechanics, 500, 145-167. https://doi.org/10.1017/S0022112003007092
35. Perrie, W., Meylan, M. H., Toulany, B. and Casey, M. (2022). Modelling Wave-Ice Interactions in Three-Dimensions in the Marginal Ice Zone and Validation Against Experimental Data, *This issue*
36. Rogers, W. E., Babanin, A. V., and Wang, D. W. (2012). Observation-Consistent Input and Whitecapping Dissipation in a Model for Wind-Generated Surface Waves: Description and Simple Calculations. *Journal of Atmospheric and Oceanic Technology* 29, 9, 1329-1346, https://doi.org/10.1175/JTECH-D-11-00092.1
37. Saiki, R., Mitsudera, H., Fujisaki-Manome, A., Kimura, N., Ukita, J., Toyota, T., & Nakamura, T. (2021). Mechanism of ice-band pattern formation caused by resonant interaction between sea ice and internal waves in a continuously stratified ocean. Progress in Oceanography, 190, 102474. page range. (doi)
38. Shen, H. H., Hibler III, W. D., & Leppäranta, M. (1987). The role of floe collisions in sea ice rheology. Journal of Geophysical Research: Oceans, 92(C7), 7085-7096.
39. Shen, H. (2022). Wave-in-ice: theoretical bases and field observations, *This issue*
40. Smit, P. B., Houghton, I. A., Jordanova, K., Portwood, T., Shapiro, E., Clark, D., ... & Janssen, T. T. (2021). Assimilation of significant wave height from distributed ocean wave sensors. Ocean Modelling, 159, 101738. https://doi.org/10.1016/j.ocemod.2020.101738

41. Smith, M., & Thomson, J. (2020). Pancake sea ice kinematics and dynamics using shipboard stereo video. Annals of Glaciology, 61(82), 1-11. https://doi.org/10.1017/aog.2019.35
42. Squire, V., Moore, S. Direct measurement of the attenuation of ocean waves by pack ice. Nature 283, 365–368 (1980). https://doi.org/10.1038/283365a0
43. Squire, V. A. (2018). A fresh look at how ocean waves and sea ice interact. Philosophical Transactions of the Royal Society A: Mathematical, Physical and Engineering Sciences, 376(2129), 20170342.
44. Squire, V. A. (2020). Ocean wave interactions with sea ice: A reappraisal. Annual Review of Fluid Mechanics, 52, 37-60.
45. Sutherland, G., Rabault, J., Christensen, K. H., & Jensen, A. (2019). A two layer model for wave dissipation in sea ice. Applied Ocean Research, 88, 111-118. https://doi.org/10.1016/j.apor.2019.03.023
46. Sverdrup, H. U., & Munk, W. H. (1946). Empirical and theoretical relations between wind, sea, and swell. Eos, Transactions American Geophysical Union, 27(6), 823-827. https://doi.org/10.1029/TR027i006p00823
47. Thomson, J., & Rogers, W. E. (2014). Swell and sea in the emerging Arctic Ocean. Geophysical Research Letters, 41(9), 3136-3140. https://doi.org/10.1002/2014GL059983
48. Thomson, J., Ackley, S., Girard‐Ardhuin, F., Ardhuin, F., Babanin, A., Boutin, G., ... & Wadhams, P. (2018). Overview of the arctic sea state and boundary layer physics program. Journal of Geophysical Research: Oceans, 123(12), 8674-8687. https://doi.org/10.1002/2018JC013766
49. Thomson, J., Hošeková, L., Meylan, M. H., Kohout, A. L., & Kumar, N. (2021). Spurious rollover of wave attenuation rates in sea ice caused by noise in field measurements. Journal of Geophysical Research: Oceans, 126(3), e2020JC016606. https://doi.org/10.1029/2020JC016606
50. Thomson, J. (2022). Wave propagation in the Marginal Ice Zone: connections and feedbacks within the air-ice-ocean system, *This issue*
51. Toffoli, A., Pitt, J. P. A., Alberello, A., and Bennets, L. G. (2022). Modelling attenuation of irregular wave fields by artificial ice floes in the laboratory, *This issue*
52. Toyota, T., Ishiyama, J., & Kimura, N. (2021). Measuring deformed sea ice in seasonal ice zones using l-band sar images. IEEE Transactions on Geoscience and Remote Sensing, 59(11), 9361-9381. https://doi.org/10.1109/TGRS.2020.3043335
53. Toyota, T., Arihara, Y., Waseda, T., Ito, M. and Nishioka, J. (2022). Observations of ice cakes with a drone in the southern Sea of Okhotsk, The 36th International Symposium on the Okhotsk Sea & Polar Oceans, 21-23 February 2022
54. Tulin, M. P. (1996). Breaking of ocean waves and downshifting. In Waves and Nonlinear Processes in Hydrodynamics (pp. 177-190). Springer, Dordrecht.
55. Tulin, M. P., & Waseda, T. (1999). Laboratory observations of wave group evolution, including breaking effects. Journal of Fluid Mechanics, 378, 197-232. https://doi.org/10.1017/S0022112098003255
56. Voermans, J. J., Babanin, A. V., Thomson, J., Smith, M. M., & Shen, H. H. (2019). Wave attenuation by sea ice turbulence. Geophysical Research Letters, 46(12), 6796-6803. https://doi.org/10.1029/2019GL082945
57. Voermans, J. J., Liu, Q., Marchenko, A., Rabault, J., Filchuk, K., Ryzhov, I., Heil, P., Waseda, T., Nose, T., Kodaira, T., Li, J., and Babanin, A. V.: (2021) Wave dispersion and dissipation in landfast ice: comparison of observations against models, The Cryosphere, 15, 5557–5575, https://doi.org/10.5194/tc-15-5557-2021
58. Wadhams, P. (1975). Airborne laser profiling of swell in an open ice field. Journal of Geophysical Research, 80(33), 4520-4528. https://doi.org/10.1029/JC080i033p04520
59. Wadhams, P. (1986). The Seasonal Ice Zone. In: Untersteiner, N. (eds) The Geophysics of Sea Ice. NATO ASI Series. Springer, Boston, MA. https://doi.org/10.1007/978-1-4899-5352-0_15
60. Wadhams, P., Squire, V. A., Goodman, D. J., Cowan, A. M., & Moore, S. C. (1988). The attenuation rates of ocean waves in the Marginal Ice Zone. Journal of Geophysical Research, 93(C6), 6799–6818.
61. Waseda, T., Kinoshita, T., & Tamura, H. (2009). Interplay of resonant and quasi-resonant interaction of the directional ocean waves. Journal of Physical Oceanography, 39(9), 2351-2362. https://doi.org/10.1175/2009JPO4147.1

62. Waseda, T., Sinchi, M., Kiyomatsu, K. et al. Deep water observations of extreme waves with moored and free GPS buoys. Ocean Dynamics 64, 1269–1280 (2014). https://doi.org/10.1007/s10236-014-0751-4
63. Weber, J. E. (1987). Wave attenuation and wave drift in the Marginal Ice Zone. Journal of physical oceanography, 17(12), 2351-2361. https://doi.org/10.1175/1520-0485(1987)017<2351:WAAWDI>2.0.CO;2
64. Wessel, P., and Smith, W. H. F. (1996), A global, self-consistent, hierarchical, high-resolution shoreline database, *J. Geophys. Res.*, 101( B4), 8741– 8743, https://doi.org/10.1029/96JB00104
65. Zieger S., Babanin, A. V., Rogers, W. E., and Young, I. R. (2015). Observation-based source terms in the third-generation wave model WAVEWATCH, *Ocean Modelling* 96, 1, 2-25, https://doi.org/10.1016/j.ocemod.2015.07.014

# Tables

Table 1: Observed integrated wave parameters from the stereo image and the buoy on ice.

| | $H_s$ | $T_p$ | $f_p$ | $\lambda_p$ (open) | $ak_p$ | *direction* |
|---|---|---|---|---|---|---|
| Stereo image | 0.34 m | 9.5 s | 0.105 Hz | 140 m | 0.0076 | n/a |
| Buoy-on-ice | 0.25 m | 14.6 – 17.1 s | 0.059-0.066 Hz | 333-456 m | 0.0017-0.0024 | ~60 deg. |

Table 2: Locations and times that the TodaiWW3-OK directional spectra were extracted. The derived integral parameters, significant wave height $H_s$, peak frequency $f_p$, peak period $T_p$, and energy period $T_{0m1}$ are listed.

| | buoy-on-ice | 90 km (Stereo camera) | 180 km | 270 km |
|---|---|---|---|---|
| lon/lat | 143.59/44.88 | 144.66/45.27 | 145.8/45.64 | 147.00/46.00 |
| time | 2/12 9:00 | 2/12 6:00 | 2/12 3:00 | 2/12 0:00 |
| $H_s$ | 0.500 m | 0.699 m | 1.26 m | 1.63 m |
| $f_p$ | 0.08 Hz | 0.08 Hz | 0.08 Hz | 0.088 Hz |
| $T_p$ | 12.5 s | 12.5 s | 12.5 s | 11.3 s |
| $T_{0m1}$ | 12.7 s | 12.2 s | 9.58 s | 9.22 s |

# Figure and table captions

Table 1: Observed integrated wave parameters from the stereo image and the buoy on ice.

Table 2: Locations and times that the TodaiWW3-OK directional spectra were extracted. The derived integral parameters, significant wave height $H_s$, peak frequency $f_p$, peak period $T_p$, and energy period $T_{0m1}$ are listed.

Figure 1: Daily AMSR2-derived Sea Ice Concentration (SIC) from Feb 12 (top left) to Feb 15 (bottom right). The colour shading changes at every 0.05 SIC. The horizontal axis is longitude and the vertical axis is latitude.

Figure 2: The ALOS-2/PALSAR image obtained on 10 Feb. 2020, is placed in the centre providing an overview of the sea ice distribution. The white dotted line traces the ship track of PV Soya from 9 Feb. to 15 Feb. 2020. The wave buoy was deployed on ice on 10 Feb. at the large solid redpoint and drifted freely to the south until the end of March when it lost connection in the Nemuro Strait (see the traces of red dots). The 12 Feb. wave event was observed at the points indicated in cyan. Stereo images were taken on the same day at a location indicated by yellow solid dot. The sea ice condition varied a lot as depicted by the four

drone images taken at locations 1 to 4 marked by yellow open circles. The magenta points are located along the 65-degree line from the buoy-on-ice (cyan points) and indicate where the directional spectra from TodaiWW3-OK were extracted. TodaiWW3-OK was forced by AMSR2-derived sea ice concentration indicated by the green contour lines.

Figure 3 (a) Spotter buoy (SOFAR) was placed on an ice floe that was broken off from a larger ice floe. (b) A sample stereo image pair was taken from the upper deck of PV Soya.

Figure 4: Buoy-on-ice derived a) significant wave height; b) mean and peak wave period; c) propagation direction; d) directional spread; e) averaged spectral energy density ($m^2s$) from the 7 spectra; and f) evolution of spectral energy density from 2020.2.11 21:30-2.12 14:00 (UTC), from bottom to top every 3 hours. The frequency resolution is 0.0098 Hz. The corresponding significant wave heights are 0.155 m, 0.20 m, 0.24 m, 0.21 m, 0.27 m, 0.24 m, and 0.25 m.

Figure 5: Stereo camera image sequences were analyzed to estimate the surface elevation time series for the two cases, 2020/2/10 07:48 and 2020/2/12/ 13:48. The top two figures (a and b) are sample time series from the estimate. Reconstruction of the surface elevation was successfully made, and the Fourier spectral densities were estimated as an ensemble average of those points; c) black for the 2/10 case and red for the 2/12 case. d) The selected 9-time series were used to estimate the directional spectral density.

Figure 6: Directional spectra (top row) extracted from the TodaiWW3-OK at locations and times indicated in Table 2. The derived frequency spectral density ($m^2s$) are shown in the bottom row.

Figure 7: Attenuation of observed wave spectral energy density by various exponential attenuation coefficients: $A = K_n f^n$ with $n = 2.0, 2.7, 3.5, 4.0$, and empirical formulas summarized in Thomson et al. (2021), CODA 2019, SeaState 2015, SIPEX 2012, STiMPI 2000, Greenland Sea 1978. The observed buoy-on-ice spectral energy density is presented in a red solid line.

Figure 8: Attenuation of simulated wave spectral densities by various exponential attenuation coefficients: $A = Kf^n$ with $n = 2.0, 2.7, 3.5, 4.0$, and empirical formulas summarized in Thomson et al. (2021), CODA 2019, SeaState 2015, SIPEX 2012, STiMPI 2000, Greenland Sea 1978. The initial condition from TodaiWW3-OK was 180 km away from the buoy location and TodaiWW3-OK spectral density at the buoy-on-ice observation point are plotted in black thick solid lines. Spectral energy density values are given in $m^2s$.